



# Composition optimization of multilayered chromium-nitride–carbon film on 316L stainless steel as bipolar plates for proton exchange membrane fuel cells

Peiyun Yi<sup>a</sup>, Linfa Peng<sup>a,\*</sup>, Tao Zhou<sup>a</sup>, Jiaqiang Huang<sup>a</sup>, Xinmin Lai<sup>a,b</sup>

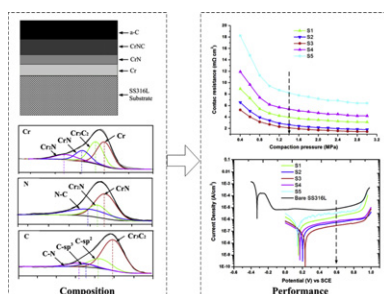
<sup>a</sup>State Key Laboratory of Mechanical System and Vibration, Shanghai Jiao Tong University, Shanghai 200240, PR China

<sup>b</sup>Shanghai Key Laboratory of Digital Manufacture for Thin-walled Structures, Shanghai Jiao Tong University, Shanghai 200240, PR China

## HIGHLIGHTS

- The composition of Cr–N–C film has great influence on coated bipolar plates.
- S3 with OEM setting of 60% achieves optimal film composition.
- Contact resistance of S3 is  $2.11 \text{ m}\Omega \text{ cm}^{-2}$  at 1.4 MPa.
- Corrosion current density of S3 is  $0.308 \mu\text{A cm}^{-2}$  in cathodic environment.

## GRAPHICAL ABSTRACT



## ARTICLE INFO

### Article history:

Received 14 December 2012

Received in revised form

11 February 2013

Accepted 13 February 2013

Available online 21 February 2013

### Keywords:

Chromium-nitride–carbon film  
Composition optimization  
Stainless steel bipolar plate  
Proton exchange membrane fuel cell  
Closed field unbalanced magnetron sputter ion plating

## ABSTRACT

The composition of multilayered chromium-nitride-carbon (Cr–N–C) film has great influence on the performance of coated 316L stainless steel (SS316L) as bipolar plates for proton exchange membrane fuel cells (PEMFCs). In this study, five films with different composition are deposited by closed field unbalanced magnetron sputter ion plating (CFUBMSIP) and the influence of nitrogen content adjusted by a closed-loop optical emission monitor (OEM) is evaluated. The phase structure and chemical composition of the films are characterized by X-ray diffractometry (XRD) and X-ray photoelectron spectroscopy (XPS). Interfacial contact resistance (ICR) between coated samples and gas diffusion layer (GDL) is measured. Potentiodynamic and potentiostatic tests are conducted to evaluate the corrosion resistance of coated samples. Experimental results show that Cr–N–C film with OEM setting of 60% presents the best performance, i.e. the ICR reduces to  $2.11 \text{ m}\Omega \text{ cm}^2$  under a compaction pressure of 1.4 MPa, and the corrosion current density reaches  $0.308 \mu\text{A cm}^{-2}$  in the PEMFCs cathodic environment ( $0.5 \text{ M H}_2\text{SO}_4 + 5 \text{ ppm HF}$  solution at  $70^\circ\text{C}$ ,  $0.6 \text{ V vs. SCE}$ ). Therefore, this study indicates that Cr–N–C film with OEM setting of 60% achieves optimal film composition and may be practically applied for commercialization of PEMFCs technology.

© 2013 Elsevier B.V. All rights reserved.

## 1. Introduction

The bipolar plate is considered to be one of the key components of proton exchange membrane fuel cells (PEMFCs) stack due to the functions of constituting the backbone, distributing reactants,

carrying current and facilitating water and thermal management through the cell etc. [1–3]. An ideal material for bipolar plate should possess the properties of good electrical conductivity, high corrosion resistance, high mechanical strength, light weight and low cost [4]. 316L stainless steel (SS316L) exhibits most of the characteristics and is extensively considered to be an alternative bipolar plate material [5,6]. Nevertheless, the corrosion resistance of bare SS316L is still far from satisfactory in the acidic (pH 2–3),

\* Corresponding author. Tel.: +86 21 34206785 (office); fax: +86 21 34204542.

E-mail addresses: [yipeiyun@gmail.com](mailto:yipeiyun@gmail.com), [penglinfa@sjtu.edu.cn](mailto:penglinfa@sjtu.edu.cn) (L. Peng).

humid, and warm (65–90 °C) PEMFCs environment [7,8]. Corrosion products of the bipolar plate would contaminate the catalysts and poison the proton exchange membrane, and form a passivation layer leading to an increase of interfacial contact resistance (ICR) between bipolar plate and gas diffusion layer (GDL) as well [9,10]. Depositing anticorrosive and conductive coatings on SS sheet is a feasible and promising way to improve its corrosion resistance giving consideration to ICR using different techniques [11].

On the one hand, the carbon-based film, possessing good conductive performance due to high fraction of C–sp<sup>2</sup> bond, has drawn worldwide attention. As summarized in Table 1, many attempts were conducted to develop the carbon-based film using different approaches, including pure carbon film, amorphous carbon (a-C) film, and chromium–carbon (Cr–C) film. In the aspect of pure carbon film, Fukutsuka et al. [12,13] prepared a carbon coating on SS304 by plasma-assisted chemical vapor deposition (CVD) method and factors affecting the formation of carbon film were investigated in detail later on [14]. Chung et al. [15] also adopted CVD method to deposit carbon film on metallic bipolar plates and illustrated similar performance improvement of coated bipolar plates. Afshar et al. [16] and Larijan [17] produced pure carbon films on polished SS316L by magnetron sputtering physical vapor deposition (MS-PVD) technique. Mori et al. [18] deposited amorphous carbon (a-C) film on the SS316L bipolar plates using an electron cyclotron resonance plasma sputtering (ECR-PS) method. In our previous work [19], a-C coating was deposited by closed field unbalanced magnetron sputter ion plating (CFUBMSIP). The *ex-situ* and *in-situ* experiments indicated significant performance improvement in ICR, corrosion resistance and durability. In the aspect of Cr–C film, Fu et al. [20] and Wu et al. [21] used arc ion plating (AIP) method to prepare Cr–C film on SS316L substrate. The Cr–C film showed very low ICR and the potentiodynamic as well as potentiostatic polarization results revealed the enhancement of corrosion resistance.

On the other hand, metal nitride films, including chromium nitride (CrN), titanium nitride (TiN), tantalum nitride (TaN) and multi-element combinations as listed in Table 1, have been widely investigated for PEMFCs applications in recent years. CrN films were mainly produced by PVD [22,23] and AIP [4,24,25] methods. The authors reported promising current conductivity and corrosion resistance. In order to improve the performance further, multilayered CrN/Cr films were developed by Tian et al. [26], Zhang et al. [27] and Park et al. [28] using PVD, AIP and unbalanced magnetron DC sputtering (UMDCS) methods, respectively. The multilayered film exhibited superior corrosion resistance and lower ICR attributed to the high adhesion force of the smooth and dense coating

and synergistic function of multilayer structure. Besides, TiN film developed by PVD [29] and AIP [30,31] exhibited similar performance enhancement. Choe et al. [32] produced TaN film on SS316L by inductively coupled plasma-assisted reactive magnetron sputtering (ICP-ARMS) at various N<sub>2</sub> flow rates. Wang et al. [33] prepared a niobium nitride (NbN) diffusion coating on SS304 via plasma surface diffusion alloying (PSDA) method.

A novel multilayered chromium-nitride–carbon (Cr–N–C) film has been demonstrated to possess strong adhesion strength, low interfacial contact resistance (ICR) and high corrosion resistance in our previous work [34]. However, the composition of multilayered Cr–N–C has great influence on the performance of coated 316L stainless steel (SS316L) as bipolar plates for PEMFCs. In the present study, a series of chromium-nitride–carbon (Cr–N–C) multilayer films with different composition were deposited on 0.1 mm thick SS316L as bipolar plates for PEMFCs via CFUBMSIP. The crystallographic structures and chemical composition of Cr–N–C films were investigated by X-ray diffractometry (XRD) and X-ray photoelectron spectroscopy (XPS), respectively. ICR and corrosion resistance of the coated samples which are closely related to the performance of PEMFCs were systematically investigated as well. The influence of film composition to the performance of coated bipolar plates is preliminarily analyzed.

## 2. Experimental

### 2.1. Deposition apparatus and procedure

A CFUBMSIP system (UDP850/4, Teer Coatings, Ltd.) equipped with two chromium targets (99.99% purity) and two graphite targets (99.99% purity) was used to prepare Cr–N–C multilayered films on 0.1 mm thick SS316L sheet as-received. Round samples with a diameter of 60 mm were firstly cleaned *ex-situ* with distilled water and ethanol in an ultrasonic machine, and then sputtered *in-situ* by Ar<sup>+</sup> ion bombardment at a –700 V bias voltage to obtain a clean and active surface. Cr–N–C multilayer films were deposited under a base pressure of  $4 \times 10^{-4}$  Pa and total Ar + N<sub>2</sub> gas pressure of 0.4 Pa, respectively. The flow rate of Ar was settled at 30 sccm and the reactive gas of nitrogen was controlled by a closed-loop optical emission monitor (OEM) which was used to detect the plasma emission of the magnetron source during the sputtering process. It should be pointed out that a higher OEM setting corresponds to a lower flow rate of nitrogen taking part in the reaction.

Fig. 1 illustrates the schematic diagram of multilayered Cr–N–C film composition on SS316L substrate. The multilayered film is composed of pure Cr sublayer, CrN sublayer, CrNC sublayer and a-C sublayer from bottom to top and the transition between two sublayers is gradient. The depositing process can be described briefly by the following four steps. Firstly, the two Cr targets were started and the sputtering current was increased from 0 A to 4 A linearly in

**Table 1**  
A summary of carbon-based and metal nitride films on metallic bipolar plates for PEMFC.

Category	Film material	Bipolar plate material	Coating method	References
Carbon-based films	Pure carbon film	SS304 and SS316L	CVD and MS-PVD	[11–16]
	a-C film	SS304 and SS316L	ECR-PS and CFUBMSIP	[17,18]
	Cr–C film	SS316L	PBAIP	[19,20]
Metal nitride films	CrN film	Al-5083 and SS316L	PVD and AIP	[3,21–24]
	CrN/Cr film	SS316L	PVD, AIP and UMDCS	[25–27]
	TiN film	SS316L and SS410	PVD and AIP	[28–30]
	TaN film	SS316L	ICP-ARMS	[31]
	NbN film	SS304	PSDA	[32]

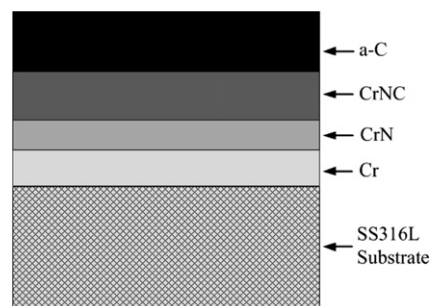


**Fig. 1.** Schematic diagram of multilayered Cr–N–C film composition on SS316L substrate (not to scale).

1 min and then kept it for 4 min to deposit a pure Cr layer. Then, the OEM was opened and kept at a setting value for 10 min to form a CrN layer. After that, two graphite targets were started and the sputtering current was set at 4 A. Meanwhile, the sputtering current of Cr targets was decreased to 3 A and kept at this value for 20 min to get a CrNC coexistence layer. Finally, the chromium targets and the OEM were closed and the sputtering current of two graphite targets was maintained at 4 A for another 20 min to produce a dense and compact a-C film. Five films, namely S1, S2, S3, S4, and S5 with OEM values of 40%, 50%, 60%, 70% and 80%, were prepared to analyze the influence of film composition to the PEMFCs-related performance of coated bipolar plates.

## 2.2. Coating evaluation

The thickness of the Cr–N–C film on SS316L sample was measured using a crater machine (BC-2, Teer Coatings, Ltd.). The evaluation of phase and texture formation was analyzed by a Rigaku D/MAX 2550 VB/PC type XRD instrument in a glancing angle mode with Cu K $\alpha$  radiation and generator settings of 40 kV and 30 mA. The atomic concentrations, chemical structural and bonding states in Cr–N–C multilayer films were inspected by XPS (AXIS Ultra DLD, Shimadzu/Kratos, Japan) with a monochromatic Al K $\alpha$  X-ray source. The pass energy used in XPS was 500 eV. Surface morphology of coated samples was carefully investigated by a field emission scanning electron microscope (FE-SEM, FEI Sirion 200).

The ICR between coated SS316L samples and simulated GDL of TGP-H-060 carbon paper was measured by a widely-used technique well documented in the literature [24]. Briefly, two pieces of GDLs were sandwiched between two copper plates and coated sample. The coated samples, GDLs and copper plates are in the same size of 60 mm in diameter. Compaction force was applied on the copper plates using a Zwick/Roell universal testing machine. A milliohm meter (ZY 9858) with a resolution of 0.1  $\mu\Omega$  was connected to copper plates and used to record the variation of total resistance. Then one piece of GDL was sandwiched between two copper plates, and the resistance of copper plates and GDL was also measured to calibrate the ICR between the Cr–N–C film and GDL. The variation in ICR was recorded as a function of the compaction pressure from 0.4 to 3.0 MPa.

The corrosion resistance of the Cr–N–C coated SS316L samples was evaluated by potentiodynamic tests in 0.5 M H<sub>2</sub>SO<sub>4</sub> + 5 ppm HF solution at 70 °C to simulate the aggressive PEMFCs environment using Corr-Test 150 Electrochemical Workstation [4]. Before recording, the samples were stabilized at open circuit potential for 30 min, and then the potential was swept from –0.6 V to 1.0 V (vs. SCE) at a scanning rate of 1 mV s<sup>–1</sup>. The simulated solutions were bubbled thoroughly with hydrogen (99.99% purity) or air, respectively, to simulate the anodic or cathodic PEMFCs environments. Besides, potentiostatic polarizations were also conducted for over 10 h to evaluate the stability of Cr–N–C film. The current density was recorded at applied anodic (–0.1 V vs. SCE) and cathodic (+0.6 V vs. SCE) potentials for PEMFCs application as a function of scanning time [34,35].

**Table 2**  
Measurement results of film thickness for S1, S2, S3, S4 and S5.

No.	Sublayers of Cr–N–C multilayer film			Total ( $\mu\text{m}$ )
	Cr + CrN ( $\mu\text{m}$ )	CrNC ( $\mu\text{m}$ )	a-C ( $\mu\text{m}$ )	
S1	0.37	0.45	0.24	1.06
S2	0.35	0.43	0.25	1.03
S3	0.34	0.42	0.26	1.02
S4	0.34	0.41	0.24	0.99
S5	0.31	0.40	0.26	0.97

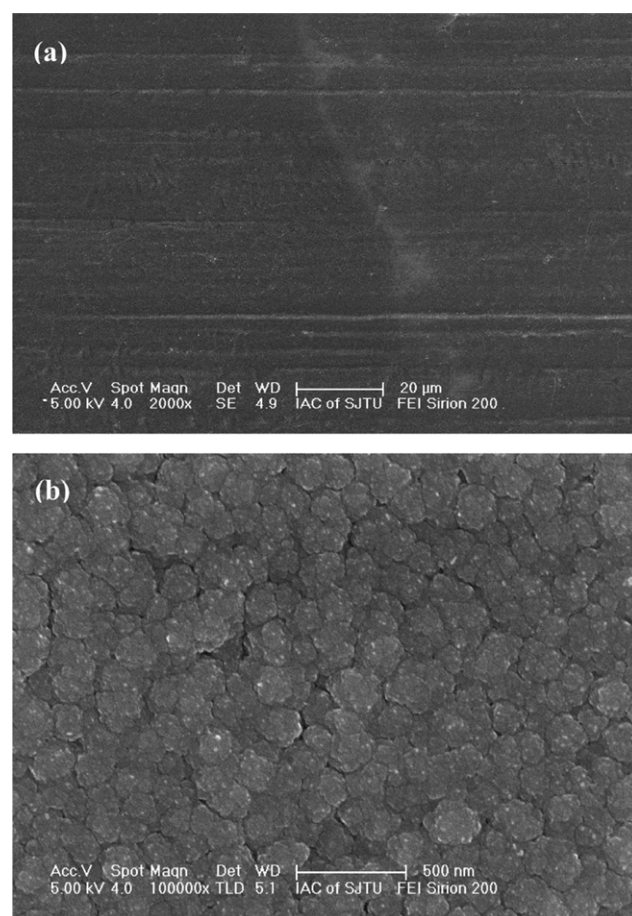


**Fig. 2.** SEM images of the surface micrograph of S1 (a) 2000 $\times$  and (b) 100,000 $\times$ .

## 3. Results and discussion

### 3.1. Thickness and surface morphology

The thickness of five Cr–N–C films on SS316L substrate was measured by a crater machine and calculated using a similar method to the literature [36]. Each sample was measured in three

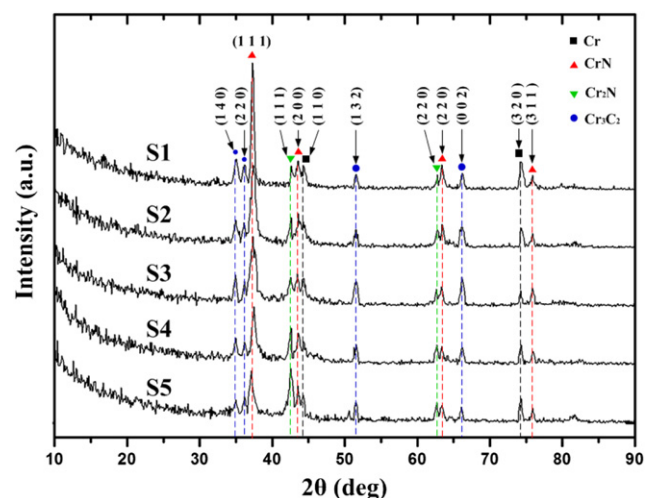


**Fig. 3.** XRD patterns of the Cr–N–C multilayer films deposited on SS316L substrate.

different locations and the average thickness is listed in Table 2. It should be pointed out that the boundary between Cr and CrN is not significant due to the small color difference and the exact thickness of Cr and CrN can hardly be obtained. Therefore, the Cr layer and CrN layer are regarded as a sublayer. The thickness of a-C layer in five films is almost the same due to the same deposition parameters. The sublayers of Cr + CrN and CrNC show a slight decrease due to the decrease of nitrogen content controlled by OEM. However, the total thickness of multilayered Cr–N–C film can be regarded to be the same within the error range.

The micrograph of multilayered Cr–N–C films on SS316L was recorded by SEM and similar surface morphology was observed for five films due to the same a-C sublayer on the surface. Therefore, only SEM images of S1 in magnification of 2000 $\times$  and 100,000 $\times$  are presented in this study. The transversal striations in Fig. 2(a) are attributed to the rolling trace of raw material because the samples are made of commercial SS316L sheet with 0.1 mm in thickness as-received without polishing. According to the SEM results, the Cr–N–C film is flat, uniform and dense and obvious pinhole is not observed in the range of observation. This is

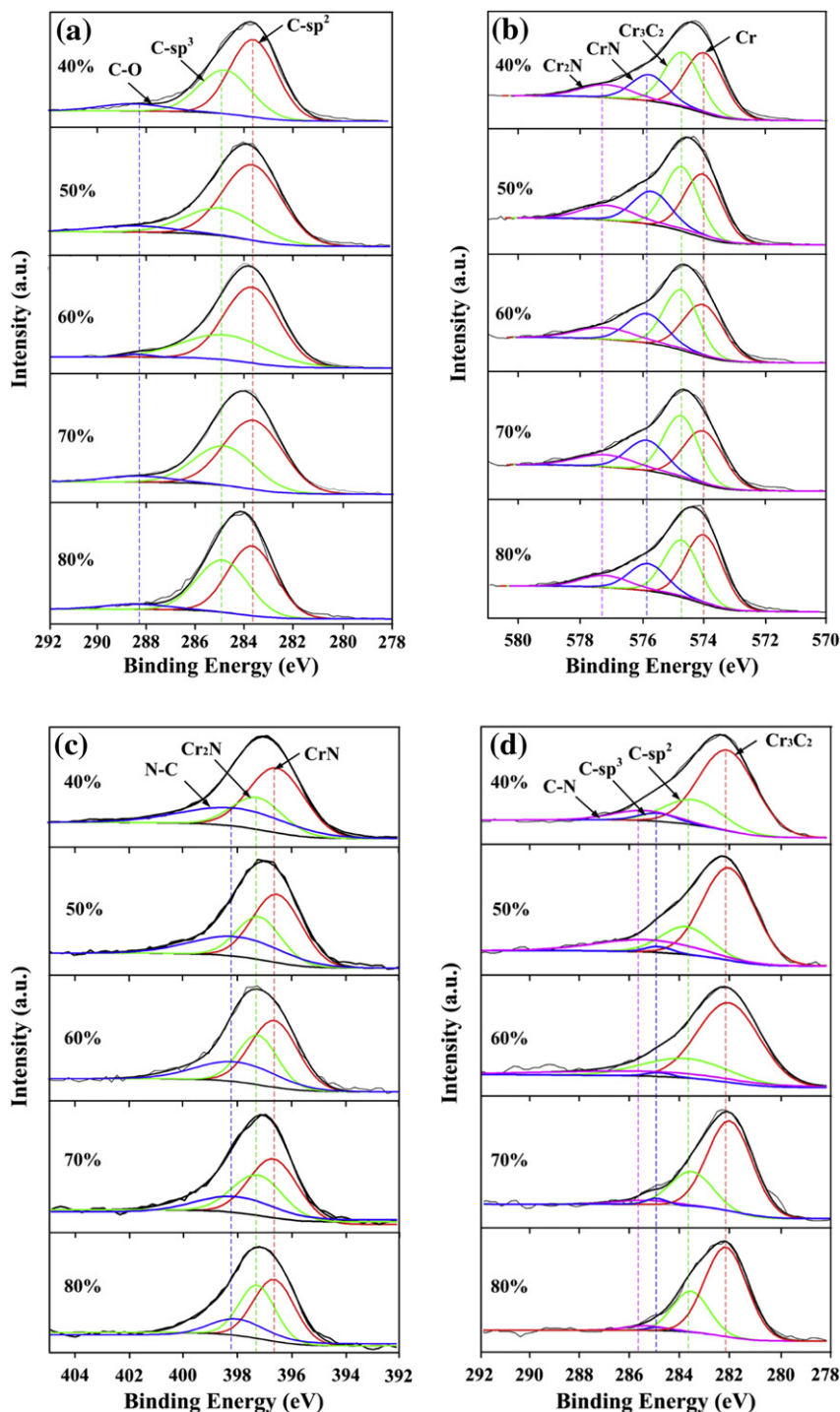


**Fig. 4.** Fitting spectra by XPS for multilayered Cr–N–C films with OEM setting of 40%, 50%, 60%, 70% and 80% (a) C1s peak of a-C sublayer (b) Cr2p3 peak of CrNC sublayer (c) N1s peak of CrNC sublayer and (d) C1s peak of CrNC sublayer.

beneficial to prevent the substrate from direct corrosion in PEMFCs environment.

### 3.2. Crystallographic structure by XRD

The crystallographic structure of five Cr–N–C films deposited on SS316L sheet was analyzed with glancing angle XRD patterns and the results are presented in Fig. 3. To avoid the influence of the substrate, a glancing angle of  $2^\circ$  was used while recording the X-ray diffraction patterns. It is obvious that CrN phase,  $\text{Cr}_2\text{N}$  phase,  $\text{Cr}_3\text{C}_2$  phase as well as metallic Cr phase with different diffraction peaks were observed. To be specific, diffraction peaks are corresponding to CrN at  $\sim 37.6^\circ$  (1 1 1),  $\sim 43.6^\circ$  (2 0 0),  $\sim 63.4^\circ$  (2 2 0),  $\sim 75.9^\circ$  (3 1 1), and  $\text{Cr}_2\text{N}$  at  $\sim 42.6^\circ$  (1 1 1),  $\sim 62.8^\circ$  (2 1 1) [24,25]. Chromium carbide in the form of  $\text{Cr}_3\text{C}_2$  is detected at  $\sim 35.0^\circ$  (1 4 0),  $\sim 36.2^\circ$  (2 2 0),  $\sim 51.6^\circ$  (1 3 2),  $\sim 66.2^\circ$  (0 0 2) [37]. Besides, metallic Cr with crystal planes of (1 1 0) and (3 2 0) is also observed. It can be concluded that the Cr–N–C multilayer films are consist of CrN,  $\text{Cr}_2\text{N}$ ,  $\text{Cr}_3\text{C}_2$  and Cr phases.

### 3.3. Chemical composition by XPS

For further investigation of film composition, XPS is adopted to inspect the chemical structural and bonding states of the multilayered Cr–N–C films on SS316L bipolar plate. The scanning spectra for Cr, N, C, O elements are fitted by the Lorentzian–Gaussian function with the Shirley background subtraction method. The binding energy of fitting peaks was corrected according to the literature [37–39] using calibration. Fig. 4 shows the fitting spectra by XPS for Cr–N–C coatings with different OEM settings.

Fig. 4(a) represents the XPS results of the surface layer corresponding to a-C sublayer in the schematic design of Fig. 1. The spectra of C1s peak are mainly decomposed into two species at 283.8 eV and 284.9 eV [37] which are corresponding to C– $\text{sp}^2$  and C– $\text{sp}^3$ , respectively. A third peak with much smaller intensity at higher binding energy represents the carbon oxides in the form of C=O bonds at 288.4 eV [37] attributed to the contamination on the film surface due to the air exposure. As listed in Table 3, the contents of the carbon atom in different chemical states are characterized by the ratio of the corresponding peak area and the total peak area. The results indicate clearly that carbon atom in the form of C– $\text{sp}^2$  is the major component and the aspect ratio of  $\text{sp}^2/\text{sp}^3$  changes with OEM settings. The percentage of C– $\text{sp}^2$  bonds of the five coated SS316L samples are in the order of  $\text{S3} > \text{S2} > \text{S1} > \text{S4} > \text{S5}$ . This trend may be attributed to the different composition in CrNC sublayer which is the substrate of the a-C sublayer. However, the mechanism of OEM value in inducing the composition, structure and property of the a-C film needs further investigation.

Fig. 4(b)–(d) show the spectra of Cr2p3, N1s and C1s in CrNC coexistence sublayer of five films in the thickness of  $d = 400$  nm, respectively. As shown in Fig. 4(b), the spectra of Cr2p3 are decomposed into metallic Cr (574.0 eV), CrN (575.8 eV),  $\text{Cr}_2\text{N}$  (577.2 eV),  $\text{Cr}_3\text{C}_2$  (574.7 eV) which are in accordance with XRD results discussed above [37,38]. In Fig. 4(c), the N1s peak may also be described by the three peaks of different intensities that correspond to CrN and  $\text{Cr}_2\text{N}$  centered at 396.6 eV and 397.2 eV, and C–N

at 398.1 eV [38,39], respectively. Beside, the C1s peak shown in Fig. 4(d) is fitted in to four dominant components. Different from the a-C sublayer in Fig. 4(a), the  $\text{Cr}_3\text{C}_2$  and C–N bonds are found at 282.1 eV and 285.4 eV [37,38] except for C– $\text{sp}^2$  and C– $\text{sp}^3$ , and carbon oxide is not observed in CrNC sublayer. Several preliminary conclusions can be concluded as below: (1) It is obvious that the chromium is excessive and there is plenty of metallic Cr in all films. This is due to the fact that the deposition rate of Cr is much higher than C. (2) With an increase of OEM setting, the content of CrN decreases and the content of  $\text{Cr}_2\text{N}$  increases slowly. This trend may be explained by the fact that less reactive gas of nitrogen takes part in reaction with a higher OEM value. (3) The content of C– $\text{sp}^2$  bonds in CrNC sublayer is in the order of  $\text{S5} > \text{S3} > \text{S4} > \text{S2} > \text{S1}$  which is slightly different from that in a-C sublayer. (4) The content of  $\text{Cr}_3\text{C}_2$  is in the order of  $\text{S3} > \text{S2} > \text{S4} > \text{S1} > \text{S5}$ .

### 3.4. Interfacial contact resistance

The contact resistance between the interface of Cr–N–C coated SS316L sample and simulated GDL of Toray TGP-H-060 carbon paper under a compaction pressure ranging from 0.4 to 3.0 MPa are presented in Fig. 5. All the Cr–N–C coated SS316L samples show quite low ICR due to the a-C film on the surface of multilayered films containing numerous disarranged graphite structures which has superior electrical performance [19]. The ICR of five films is in the range from  $2.11 \text{ m}\Omega \text{ cm}^2$  to  $8.23 \text{ m}\Omega \text{ cm}^2$  at a compaction force of 1.4 MPa. Nevertheless, the ICR results show slight difference between the five films and they are in the order of  $\text{S3} < \text{S2} < \text{S1} < \text{S4} < \text{S5}$ . This trend is in reverse order of C– $\text{sp}^2$  content in a-C sublayer of five films discussed in Fig. 4(a) and Table 2. It is obvious that the higher the C– $\text{sp}^2$  content in the a-C sublayer, the lower ICR achieves for the coated SS316L bipolar plates. This phenomenon is consistent with the results reported by many other researchers [14,21]. In summary, the film of S3 with OEM value of 60% achieves lowest ICR of  $2.11 \text{ m}\Omega \text{ cm}^2$  at 1.4 MPa which is much lower than the DOE's 2020 technical target of  $10 \text{ m}\Omega \text{ cm}^2$ .

### 3.5. Electrochemical behavior

Potentiodynamic and potentiostatic tests are commonly used approaches to evaluate the electrochemical behavior of the coatings for PEMFCs application. Fig. 6 presents the potentiodynamic polarization curves of S1, S2, S3, S4, S5 as well as bare SS316L in the

**Table 3**  
Contents of carbon atoms in different chemical states for a-C sublayers of S1, S2, S3, S4 and S5 (at%).

No.	S1	S2	S3	S4	S5
C– $\text{sp}^2$	59.1	64.4	66.5	57.7	52.4
C– $\text{sp}^3$	34.9	28.3	29.4	34.9	42.3
C=O	6.0	7.3	4.1	7.4	5.3

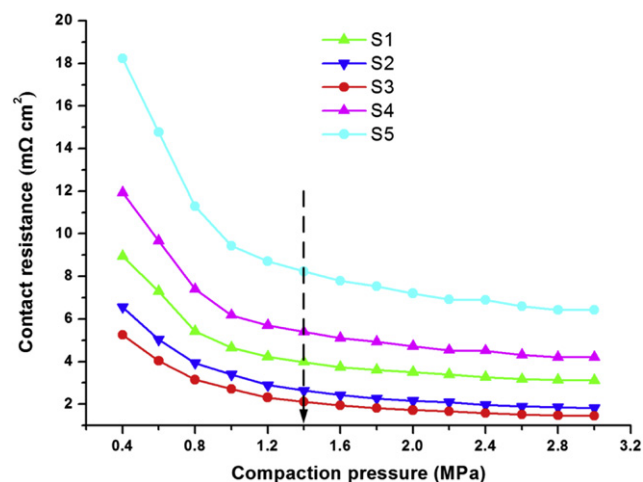
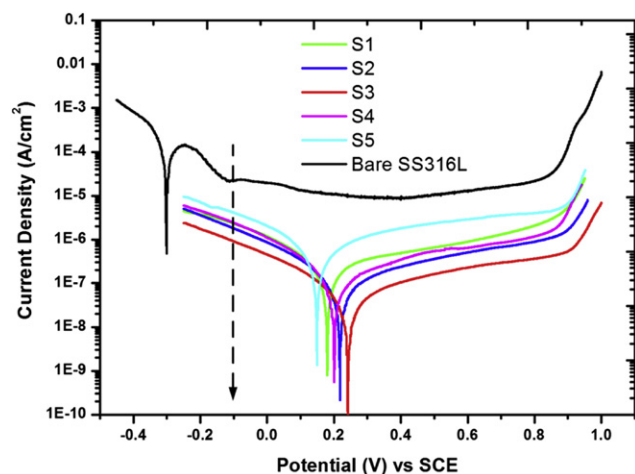


**Fig. 5.** Interfacial contact resistance of Cr–N–C coated SS316L samples with Toray TGP-H-060 carbon paper.

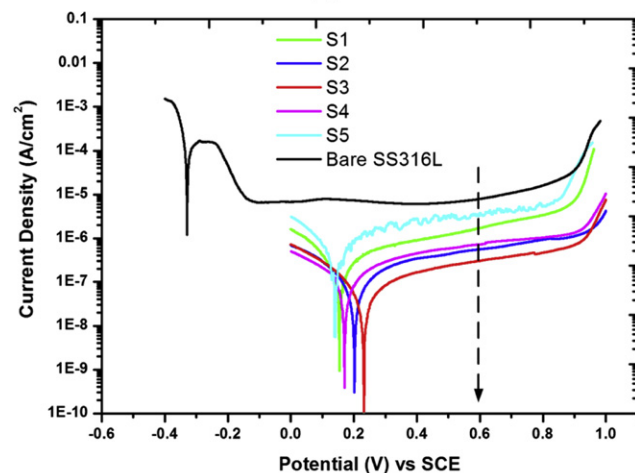
simulated anodic and cathodic environments. Compared to bare SS316L, all the Cr–N–C coated samples show much lower corrosion current densities in both anodic and cathodic environments revealing that the substrate is protected by the coatings. More specifically, the corrosion potentials of the S1, S2, S3, S4 and S5 shown in Fig. 6(a) reach about 0.180 V, 0.218 V, 0.242 V, 0.201 V, and 0.152 V respectively. All of them are more positive than the operation potential in the PEMFCs anodic environment (around  $-0.1$  V vs. SCE). Thermodynamically, a higher corrosion potential indicates higher chemical inertness and better corrosion resistance. Therefore, the corrosion resistance of five Cr–N–C films in anodic PEMFCs environment is in the order of  $S3 > S2 > S4 > S1 > S5$ . This trend is also observed in the simulated cathodic environment as shown in Fig. 6(b). The passivation current densities of coated SS316L samples in the PEMFCs cathodic environment (about  $+0.6$  V vs. SCE), which are marked with a vertical line, are  $1.72 \mu\text{A cm}^{-2}$ ,  $0.561 \mu\text{A cm}^{-2}$ ,  $0.308 \mu\text{A cm}^{-2}$ ,  $0.726 \mu\text{A cm}^{-2}$  and  $3.75 \mu\text{A cm}^{-2}$ , respectively. Combining the potentiodynamic tests in anodic and cathodic environments, the corrosion resistance of Cr–N–C film is closely related to the film composition and in the order of  $S3 > S2 > S4 > S1 > S5$ . Only S2,

S3 and S4 with OEM value of 50%, 60% and 70% meets the DOE's 2020 technical target of  $1.0 \mu\text{A cm}^{-2}$ .

Potentiostatic tests were also conducted for S1, S2, S3, S4, S5 as well as bare SS316L to further investigate the durability of the Cr–N–C film in simulated corrosive solution at  $70^\circ\text{C}$  for over 10 h. The current density was recorded at applied anodic ( $-0.1$  V vs. SCE) and cathodic ( $+0.6$  V vs. SCE) potentials as a function of operating time and the results are presented in Fig. 7. As shown in Fig. 7(a), the current density obtained from the uncoated sample decreases in the beginning and then increases to a relatively high level. This trend is also observed by other researchers [9,21]. However, the current densities measured from five Cr–N–C coated SS316L samples exhibit different phenomena. They decrease in the beginning and gradually stabilize at a lower current density of about  $10^{-6.0} \text{ A cm}^{-2}$ ,  $10^{-6.5} \text{ A cm}^{-2}$ ,  $10^{-6.8} \text{ A cm}^{-2}$ ,  $10^{-6.4} \text{ A cm}^{-2}$  and  $10^{-5.9} \text{ A cm}^{-2}$  for S1, S2, S3, S4 and S5, respectively, which are much lower than that of bare sample. As shown Fig. 7(b), the current densities acquired for Cr–N–C coated samples in simulated cathodic environment decrease rapidly initially and then gradually stabilize at about  $10^{-7.2} \text{ A cm}^{-2}$ ,  $10^{-7.7} \text{ A cm}^{-2}$ ,  $10^{-7.8} \text{ A cm}^{-2}$ ,  $10^{-7.5} \text{ A cm}^{-2}$  and  $10^{-6.9} \text{ A cm}^{-2}$  respectively.

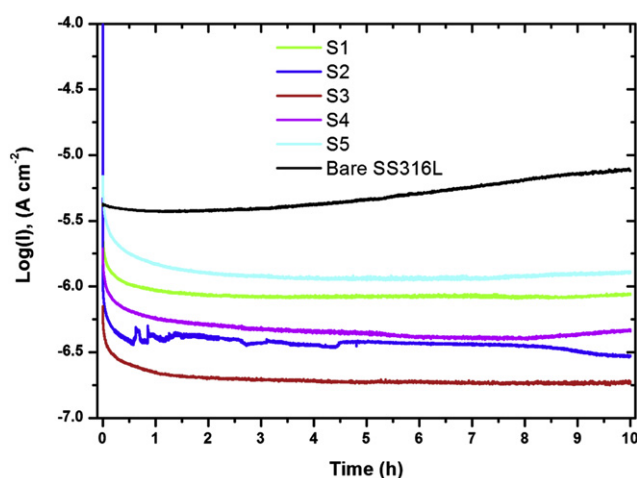


(a)

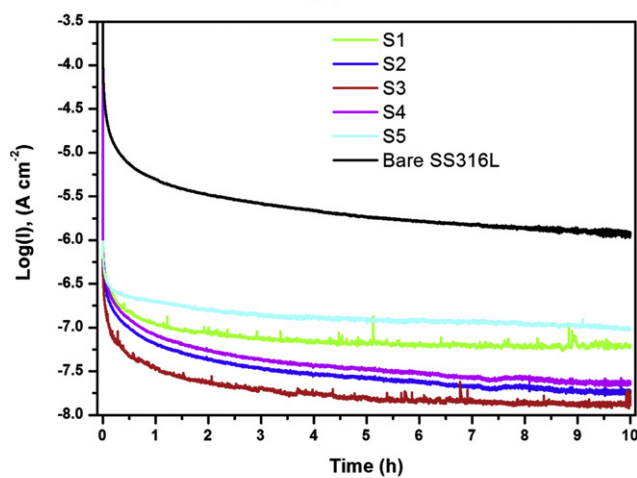


(b)

Fig. 6. Polarization behaviors of the Cr–N–C coated and bare SS316L samples in  $0.5 \text{ M H}_2\text{SO}_4 + 5 \text{ ppm HF}$  solution with a scan rate of  $1 \text{ mV s}^{-1}$  at  $70^\circ\text{C}$  (a) anodic behavior aerated with  $\text{H}_2$  and (b) cathodic behavior bubbled with air.



(a)



(b)

Fig. 7. Potentiostatic behaviors of the Cr–N–C coated and bare SS316L samples (a) simulated anodic ( $-0.1$  V vs. SCE, purged with  $\text{H}_2$ ) and (b) cathodic environment ( $+0.6$  V vs. SCE, bubbled with air).

Combining the potentiodynamic and potentiostatic results, it can be concluded that the corrosion resistance of five Cr–N–C samples with different composition is in the order of  $S3 > S2 > S4 > S1 > S5$ . This trend is in accordance with the  $Cr_3C_2$  content in CrNC sublayer as described in Fig. 4. It seems that the film with a higher  $Cr_3C_2$  content achieves lower corrosion current density. This phenomenon may be attributed to the fact that Cr–C film achieves higher corrosion resistance than CrN film demonstrated by published results [21,24]. In summary, the film of S3 with OEM value of 60% achieves best anticorrosion performance with corrosion potential of 0.242 V in anodic environment and corrosion current density of  $0.308 \mu A cm^{-2}$  in cathodic environment.

#### 4. Conclusion

The influence of multilayered Cr–N–C film compositions on the performance of coated 316L bipolar plates for PEMFCs has been experimentally investigated. Five films with different nitrogen contents are deposited on 0.1 mm thick SS316L sheets via CFUBMSIP through adjusting the OEM setting of 40%, 50%, 60%, 70% and 80%. The crystallographic structures and chemical composition of Cr–N–C films were investigated by XRD and XPS. The performance of Cr–N–C coated SS316L is significantly improved compared to the bare SS316L. The ICR between the coated SS316L sheets and GDL is in the order of  $S3 < S2 < S1 < S4 < S5$ , which is consisted with the content of C-sp<sup>2</sup> in the a-C sublayer, and the ICR of S3 is only  $2.11 m\Omega cm^2$  at 1.4 MPa. The corrosion resistance of Cr–N–C film is in the order of  $S3 > S2 > S4 > S1 > S5$  which is closely related to the  $Cr_3C_2$  content in the CrNC sublayer. The corrosion potential of five films is more positive than the operation potential in the PEMFCs anodic environment and S3 achieves lowest corrosion resistance of  $0.308 \mu A cm^{-2}$  in the cathodic environment. It is concluded that the ICR performance is mainly decided by the content of C-sp<sup>2</sup> in a-C sublayer and the corrosion resistance is mainly depended on the content of  $Cr_3C_2$  in CrNC sublayer. The film of S3 with OEM setting of 60% achieves optimal film composition and can be practically applied for commercialization of PEMFCs technology. However, the coating process parameters, i.e. the sputtering current and sputtering time, can further optimized to improve the content of C-sp<sup>2</sup> and  $Cr_3C_2$  and decrease the content of metallic Cr to achieve higher performance in the future.

#### Acknowledgment

This work was carried out within the projects supported by the National Natural Science Foundation of China (Nos. 51235008, 51275294, 51121063, and 50930005), and China Postdoctoral Science Foundation Grant (No. 2012M520888). It was also supported by National High Technology Research and Development Program of China (“863” program, Nos. 2011AA11A271, 2013AA110201) and the Program of Introducing Talents of Discipline to Universities (No. B06012). Finally, the authors would like to thank Prof. Xun Cai from the School of Materials Science and Engineering, SJTU for helpful discussions.

#### References

- [1] Y. Wang, K.S. Chen, J. Mishler, S.C. Cho, X.C. Adroher, Appl. Energy 88 (2011) 981–1007.
- [2] D.Q. Mei, M. Qian, B.H. Liu, B. Jin, Z.h. Yao, Z.C. Chen, J. Power Sources 205 (2012) 367–376.
- [3] Y. Yu, Z.K. Tu, Z.G. Zhan, M. Pan, Int. J. Energy Res. 36 (2012) 845–855.
- [4] Y. Fu, G.Q. Lin, M. Hou, B. Wu, H.K. Li, L.X. Hao, Z.G. Shao, B.L. Yi, Int. J. Hydrogen Energy 34 (2009) 453–458.
- [5] S. Karimi, N. Fraser, B. Roberts, F.R. Foulkes, Adv. Mater. Sci. Eng. 2012 (2012) 1–22.
- [6] H. Wang, J.A. Turner, Fuel Cells 10 (2010) 510–519.
- [7] Z.K. Tu, H.N. Zhang, Z.P. Luo, J. Liu, Z.M. Wan, M. Pan, J. Power Sources 222 (2013) 277–281.
- [8] Z.M. Wan, J. Liu, Z.P. Luo, Z.K. Tu, Z.C. Liu, W. Liu, Appl. Energy 104 (2013) 751–757.
- [9] M. Zhang, B. Wu, G.Q. Lin, Z.G. Shao, M. Hou, B.L. Yi, J. Power Sources 196 (2011) 3249–3254.
- [10] H. Tang, S. Peikang, S.P. Jiang, F. Wang, M. Pan, J. Power Sources 170 (2007) 85–92.
- [11] R.A. Antunes, M.C.L. Oliveira, G. Ett, V. Ett, Int. J. Hydrogen Energy 35 (2010) 3632–3647.
- [12] T. Fukutsuka, T. Yamaguchi, S.-I. Miyano, Y. Matsuo, Y. Sugie, Z. Ogumi, J. Power Sources 174 (2007) 199–205.
- [13] T. Fukutsuka, T. Yamaguchi, Y. Matsuo, Y. Sugie, Z. Ogumi, Electrochemistry 75 (2007) 152–154.
- [14] Y. Matsuo, S. Miyano, Y. Sugie, T. Fukutsuka, J. Fuel Cell. Sci. Technol. 8 (2011). 031008–031001–031005.
- [15] C.-Y. Chung, S.-K. Chen, P.-J. Chiu, M.-H. Chang, T.-T. Hung, T.-H. Ko, J. Power Sources 176 (2008) 276–281.
- [16] A. Afshar, M. Yari, M.M. Larijani, M. Eshghabadi, J. Alloy Compd. 502 (2010) 451–455.
- [17] M.M. Larijani, M. Yari, A. Afshar, M. Jafarian, M. Eshghabadi, J. Alloy Compd. 509 (2011) 7400–7404.
- [18] Y. Mori, M. Ueda, M. Hashimoto, Y. Aoi, S. Tanase, T. Sakai, Surf. Coat. Technol. 202 (2008) 4094–4101.
- [19] P.Y. Yi, L.F. Peng, L.Z. Feng, P. Gan, X.M. Lai, J. Power Sources 195 (2010) 7061–7066.
- [20] Y. Fu, G.Q. Lin, M. Hou, B. Wu, Z. Shao, B. Yi, Int. J. Hydrogen Energy 34 (2009) 405–409.
- [21] B. Wu, G.Q. Lin, Y. Fu, M. Hou, B.L. Yi, Int. J. Hydrogen Energy 35 (2010) 13255–13261.
- [22] J. Barranco, F. Barreras, A. Lozano, M. Maza, J. Power Sources 196 (2011) 4283–4289.
- [23] O. Lavigne, C. Alemany-Dumont, B. Normand, S. Berthon-Fabry, R. Metkemeijer, Int. J. Hydrogen Energy 37 (2012) 10789–10797.
- [24] B. Wu, Y. Fu, J. Xu, G.Q. Lin, M. Hou, J. Power Sources 194 (2009) 976–980.
- [25] M. Zhang, G.Q. Lin, B. Wu, Z.G. Shao, J. Power Sources 205 (2012) 318–323.
- [26] R.J. Tian, J. Power Sources 196 (2011) 1258–1263.
- [27] H.B. Zhang, G.Q. Lin, M. Hou, L. Hu, Z.Y. Han, Y. Fu, Z.G. Shao, B.L. Yi, J. Power Sources 198 (2012) 176–181.
- [28] Y.-C. Park, S.-H. Lee, S.-K. Kim, S. Lim, D.-H. Jung, K.-B. Park, S.-Y. Choi, J.-H. Kim, D.-H. Peck, Electrochim. Acta 56 (2011) 7602–7609.
- [29] Y. Wang, D.O. Northwood, Int. J. Hydrogen Energy 32 (2007) 895–902.
- [30] R.J. Tian, J.C. Sun, Int. J. Hydrogen Energy 36 (2011) 6788–6794.
- [31] D.M. Zhang, L.T. Duan, L. Guo, W.-H. Tuan, Int. J. Hydrogen Energy 35 (2010) 3721–3726.
- [32] C. Choe, H. Choi, W. Hong, J.-J. Lee, Int. J. Hydrogen Energy 37 (2012) 405–411.
- [33] L.X. Wang, J.C. Sun, J. Sun, Y. Lv, S. Li, S.J. Ji, Z.S. Wen, J. Power Sources 199 (2012) 195–200.
- [34] P.Y. Yi, L.F. Peng, T. Zhou, H. Wu, X.M. Lai, Int. J. Hydrogen Energy 38 (2013) 1535–1543.
- [35] P.Y. Yi, L.F. Peng, T. Zhou, H. Wu, X.M. Lai, J. Power Sources 230 (2013) 25–31.
- [36] W.H. Jin, K. Feng, Z.G. Li, X. Cai, L. Yu, D.H. Zhou, J. Power Sources 196 (2011) 10032–10037.
- [37] X.C. Chen, Z.J. Peng, Z.Q. Fu, W. Yue, X. Yu, C.B. Wang, Surf. Coat. Technol. 204 (2010) 3319–3325.
- [38] A. Vyas, Y.G. Shen, Z.F. Zhou, K.Y. Li, Compos. Sci. Technol. 68 (2008) 2922–2929.
- [39] Y.J. Shi, S.Y. Long, L. Fang, S.C. Yang, F.S. Pan, Appl. Surf. Sci. 254 (2008) 5861–5867.